Journal of Photochemistry & Photobiology, A: Chemistry 440 (2023) 114648

Contents lists available at ScienceDirect

Journal of Photochemistry & Photobiology, A: Chemistry

journal homepage: www.elsevier.com/locate/jphotochem

Impact of silica nanoparticles architectures on the photosensitization of O_2 by immobilized Rose Bengal

Nathalie Body [a], Corentin Lefebvre [a], Pierre Eloy [b], Tommy Haynes [a], Sophie Hermans [a,*], Olivier Riant [a,*]

[a] Molecular Chemistry, Materials and Catalysis (MOST), Institute of Condensed Matter and Nanosciences (IMCN), Université catholique de Louvain, UCLouvain, 1, Place Louis Pasteur, 1348 Louvain-la-Neuve, Belgium

[b] Surface Characterisation Platform (SUCH) and Division Bio and Soft Matter (BSMA), Institute of Condensed Matter and Nanosciences (IMCN), Université catholique de Louvain, UCLouvain, 1, Place Louis Pasteur, 1348 Louvain-la-Neuve, Belgium

ARTICLE INFO

Keywords:
Silica nanoparticles
Morphology
Rose Bengal
Singlet oxygen
Heterogenization
Photocatalysis

ABSTRACT

Transforming light into chemical energy has been widely studied to design ecofriendly, cost-effective and sustainable synthetic approaches. The heterogenization of organic photocatalysts is a well-known strategy providing efficient solid supported catalysts. One of the most suitable solid as support is silica nanoparticles (NPs). This research note highlights the impact of silica nanoparticles morphology on a representative photochemical process that is the photooxidation of citronellol, involving oxygen sensitization. Three architectures of silica NPs were investigated: Nanospheres (NS), Core-Shell (CS) and Urchins (U). Their surfaces were functionalized with ammonium moieties allowing the immobilization of Rose Bengal (RB) by electrostatic interactions. The heterogenized RB on the various supports displayed different activities in the production of singlet oxygen, CS being the best support in terms of activity, recyclability and dye immobilization rate.

1. Introduction

The production of singlet oxygen is one of the most studied photochemical process, since the pioneer work of Foote and Wexler in 1964 [1,2]. Singlet oxygen is an important species that can be useful in photodynamic therapy, depollution or even in organic synthesis applications. It is common knowledge that the production of singlet oxygen requires a photosensitizer which absorbs UV or visible light and, after a singlet to triplet intersystem crossing, is enabled to do an energy transfer with the ground triplet state of molecular oxygen [3]. Two main classes of photosensitizers can be distinguished: metallic complexes (based on iridium or ruthenium centers) and organic dyes (e.g. Rose Bengal, Eosin, Methylene Blue) [4]. Although these catalysts are highly efficient towards singlet oxygen production, their main drawbacks are their price (especially for metals), multiple steps synthesis, tedious separation from products, photobleaching (especially for dyes) or even toxicity. To solve these problems, their immobilization on a support is an interesting strategy.

Silica nanoparticles are one of the most suitable supports for immobilizing organic photocatalysts. Since decades, silica functionalization with various moieties was developed easily and led to a broad variety of linkages to immobilize molecular species [5]. Moreover, multiple architectures have been described like nanospheres [6], magnetic particles [7], core-shell [8], hollow spheres or nanofibers [9], urchins or dendritic silica [10]… These available morphologies are a real asset for the use of silica nanoparticles. Indeed, numerous examples in the literature described the influence of the texture of inorganic photocatalysts such as TiO_2 [11–13] or ZnO [14,15] on their photocatalytic activity. It would be interesting to investigate if the morphology of the support can also have an impact on supported organic photocatalysts activity, giving therefore an active role to the support in the photocatalytic process.

To the best of our knowledge, only a few articles are dedicated to this end (Scheme 1). In 2002, Maldotti *et al.* studied the immobilization of $(n\text{-}Bu_4N)_4W_{10}O_{32}$ on MCM-41 and amorphous silica NPs. The photocatalytic activity of the decatungstate ion was influenced by the morphology of the support from both the overall yield and the chemoselectivity points of view [16]. González-Muñoz *et al.* dedicated some

* Corresponding authors.
E-mail addresses: nathalie.body@uclouvain.be (N. Body), pierre.eloy@uclouvain.be (P. Eloy), sophie.hermans@uclouvain.be (S. Hermans), olivier.riant@uclouvain.be (O. Riant).

https://doi.org/10.1016/j.jphotochem.2023.114648
Received 9 January 2023; Received in revised form 15 February 2023; Accepted 24 February 2023
Available online 27 February 2023
1010-6030/© 2023 Elsevier B.V. All rights reserved.

research efforts to the impact of the size and shape of silica NPs pores on the anchoring of a platinum complex and 10-phenylphenothiazine. They highlighted the best efficiency of SBA-15 materials thanks to an easy access to the catalyst made possible by the large pores and allowing rapid substrate diffusion, compared to MSN (hexagonal pores) and MSU (wormhole-like pores) materials [17,18]. In 2011, Mori *et al.* anchored the photocatalyst $[Ir(Mebib)(ppy)]^+$ on three different mesoporous silicas namely, SBA-15, MCM-48 and MCM-41. These materials displayed different emission intensities induced by differences in pore dimension and structure of the mesoporous silica supports meaning that the local environment can influence the excited state of the iridium complex. These heterogenized complexes were tested in the photooxidation of *trans*-stilbene and 1-naphtol for which SBA-15 was the best material in terms of photoactivity and turn-over number (TON) [19].

We describe herein the impact of nanostructured silica NPs on the production of singlet oxygen. The anchoring of Rose Bengal (RB), an efficient photosensitizer, on silica NPs has been reported in the literature for applications in photodynamic therapy [20–22] and this system is a suitable one to bring light onto the importance of the support. Furthermore, Soria-Castro *et al.* selected this chromophore for covalent grafting on ordered mesoporous silica and showed that up to eight recycling cycles of the supported catalyst was possible on a model photocatalyzed aza-Henry reaction, without any loss in photoactivity [23]. In our design, a non-covalent interaction was chosen as linkage between ammonium groups inserted at the surface and/or in pores of the support and the negative charges of RB. This allows anchoring without photosensitizer chemical modifications and should ensure optimal photocatalytic activity. The envisaged silica NPs morphologies are NanoSpheres (NS), Core-Shell (CS) and Urchins (U) (dendritic fibrous silica NPs). The heterogenized RB onto these supports are referenced as RB@NS, RB@CS and RB@U.

2. Materials and methods

2.1. Chemicals and materials

Toluene was distilled on MBraun MBSPS5 device before use. Ethanol (99 % V/V euro denaturated with 1 % of isopropanol, VWR), acetone (> 98 %, VWR), acetonitrile (HPLC-water content below 30 ppm, VWR), tetraethylorthosilicate (TEOS, ≥ 99 %, Sigma-Aldrich), ammonium hydroxide (NH_4OH, 25 % solution in water, Acros Organics), hexadecyltrimethylammonium bromide (CTAB, ≥ 99 %, Sigma-Aldrich), urchins nanoparticles (Strem, catalog reference: 14-6310), 3-(*N*,*N*-Dimethylamino)propyl]trimethoxysilane (DAPTMS, > 96 %, TCI, kept safe from air and moisture), methyl triflate ($CF_3SO_3CH_3$, 97 %, Alfa Aesar), Rose Bengal (RB, 85 %, Acros Organics, kept under dark), citronellol (>95 %, Sigma-Aldrich), triphenylphosphine (PPh_3, 99 %, Fluorochem) and dimethylsulfone (DMS, 99 %, Alfa Aesar) were used as received. Photocatalytic tests were performed using 513 nm green LEDs strips purchased from HUBO stores.

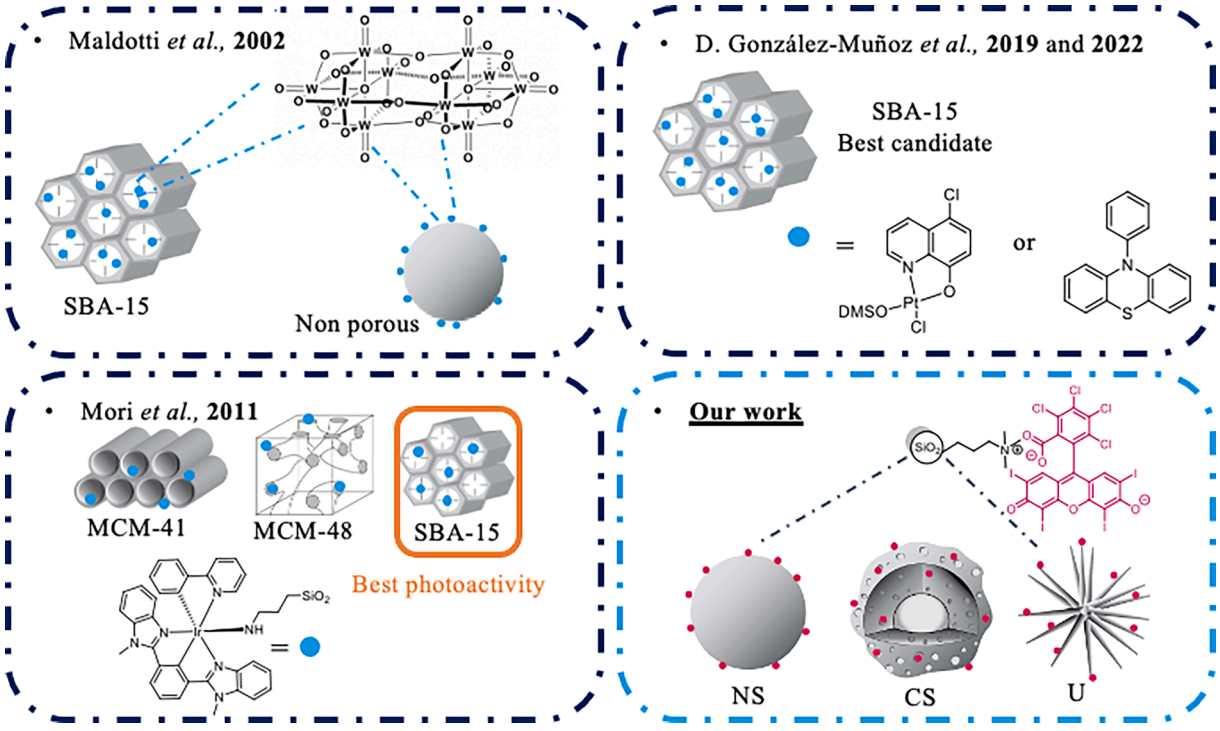
2.2. Characterization methods

NMR spectra were recorded on BRUKER spectrometers (300 MHz for ^1H). Chemical shifts are reported in δ ppm relative to the residual solvent peak for $CDCl_3$ ($\delta = 7.26$ ppm).

XPS analyses were carried out at room temperature with a SSIX-probe (SSX 100/206) photoelectron spectrometer from Surface Science Instruments (USA) equipped with a monochromatized microfocus Al X-ray source. Samples were stuck onto small sample holders with double-face adhesive tape and then placed on an insulating home-made ceramic carousel (Macor®, Switzerland). Charge effects were avoided by placing a nickel grid above the samples and using a flood gun set at 8 eV. The binding energies were calculated with respect to the Si_{2p} peak fixed at 103.5 eV. Data treatment was performed with the CasaXPS program (Casa Software Ltd., UK). The peaks were decomposed into a sum of Gaussian/Lorentzian (85/15) after subtraction of a Shirley type baseline.

UV-vis absorption spectra were recorded on a Shimadzu UV-1700 instrument using 1 cm large cuvettes in quartz.

Thermograms were recorded on a TGA/SDTA 851e simultaneous DSC-TGA instrument from METTLER TOLEDO. These analyses were carried out with a heating ramp of 10 °C/min and under air flow (100 mL/min) with the samples (3–20 mg) placed into alumina containers.



Scheme 1. Study of the silica nanostructure impact on photocatalytic processes: past and present work.

TEM images were obtained with a LEO 922 OMEGA energy filter transmission electron microscope. The powder samples were suspended in ethanol under ultrasonic treatment, then a few drops of the supernatant were deposited on a holey carbon film supported on a copper grid (Protochips, 1.2 μm hole diameter, 1.3 μm hole spacing, 200 mesh copper grid), which was dried for a few hours under vacuum at room temperature before analysis.

CHN analyses were carried out on a FlashSmart device from Thermo Scientific. The reactor temperature was set at 950 °C and the one from GC oven at 65 °C. The gas flows for vector and reference He and O_2 were 140, 100 and 250 mL/min, respectively. A packed column CHNS/NCS (PTFE, 2 m, 6X5 mm) was used with a katharometer as a detector. 1–2 mg of each samples were precisely weighed and put in a tin cupule. The quantification was based on a calibration curve (4 points).

FTIR spectra were recorded on Perkin Elmer Spectrum Two-UATR Two by depositing the powder onto the diamond equipped with a mechanical press.

A Biofuge Stratos Heraeus Instrument was used as centrifuge. 50 mL in PP tubes were purchased from VWR (525–1098).

2.3. Silica nanoparticles synthesis

Silica nanospheres – NS (40 nm) [6]. 150 mL of ethanol (99.9 % denaturated) were introduced in a 500 mL Erlenmeyer. Under vigorous stirring, 6 mL of NH_4.OH were added quickly. The reaction mixture was stirred for 5 min at room temperature. Then, 10 mL of tetraethylorthosilicate (TEOS) were added dropwise with a syringe pump at a rate of 59 mL/hour. The solution was left under stirring for 6 h at room temperature. The silica nanoparticles were recovered by centrifugation (9.500 rpm for 40 min) and washed with ethanol several times. The nanoparticles were dried in the oven at 100 °C overnight and subsequently grinded to obtain a fine white/beige powder.

Core-Shell nanoparticles – CS (50 nm) [8]. 150 mL of ethanol (99.9 % denaturated) were introduced in a 500 mL Erlenmeyer. Under vigorous stirring, 6 mL of NH_4.OH were added quickly. The reaction mixture was stirred for 5 min at room temperature. Then, 10 mL of tetraethylorthosilicate (TEOS) were added dropwise with a syringe pump at a rate of 59 mL/hour. The solution was left under stirring for 6 h at room temperature. 380 mL of Milli-Q water and 30 mL of a hexadecyltrimethylammonium bromide (CTAB) solution (1.2 g of CTAB dissolved in 20 mL H_2O/10 mL EtOH) were added and the solution was left under stirring for 30 min. 2.15 mL of TEOS were added and the mixture was stirred overnight. The silica nanoparticles were recovered by centrifugation (6000 rpm for 50 min) and subsequently dried in the oven at 100 °C. Finally, the inorganic oxide was calcinated by heating at 500 °C for 5 h at rate of 10 °C/min (3 g of silica nanoparticles were recovered).

2.4. Silica nanoparticles functionalization

Amine anchoring [24]. Nanospheres, Core-Shell, and Urchins silica nanoparticles were functionalized with the same protocol. 100 mg of silica nanoparticles were added in a 25 mL flame-dried round bottom flask and 3 cycles vacuum/argon were applied. 10 mL of dry toluene was added and the resulting suspension was sonicated for 15 min at power 3 on a VWR ultrasonic bath. [3-(*N*,*N*-Dimethylamino)propyl]trimethoxysilane (DAPTMS) (0.5 eq., 0.83 mmol, 184.2 mg, 0.19 mL) was added dropwise and the suspension was refluxed at 120 °C for 24 h. Filtration on a PVDF Millipore Membrane (0.1 μm) allowed the recovery of the solid. The white/beige powder was washed with 3X100 mL of ethanol.

Ammonium functionalization [25]. 100 mg of NMe_2-functionalized silica nanoparticles were inserted into a 25 mL flame-dried round bottom flask and 3 cycles vacuum/argon were applied. 10 mL of acetone were injected by syringe through a septum and the resulting suspension was sonicated for 15 min at power 3 on a VWR ultrasonic bath. $CF_3SO_3CH_3$ (5 eq. with regard to the number of amine functions estimated by TGA in 100 mg of NMe_2-silica nanoparticles) was added dropwise and the suspension was stirred at room temperature for 24 h during which a yellow/orange coloration was observed. Filtration on a PVDF Millipore Membrane (0.1 μm) allowed the recovery of the solid. The white/beige powder was washed with 3X100 mL of acetone.

Rose Bengal immobilization. 100 mg of NMe_3^+-functionalized silica nanoparticles were dispersed in 40 mL of Milli-Q water. Different tests of immobilization were conducted on each nanostructure to find the maximal amount of RB that the materials can immobilize (amount from which a pink filtrate was recovered meaning that an excess of RB was introduced). These amounts vary, depending on the specific surface area of the materials. We could determine that 15, 25 or 20 mg of RB (for NS, CS and U, respectively) were necessary and added to the dispersed silica nanoparticles. The dark pink mixture was stirred for 2 h at room temperature before being cooled to 0 °C. The solid was recovered by filtration on a PVDF Millipore Membrane (0.1 μm) and washed with cold DCM (2X50 mL). The solid was dried under vacuum overnight before being analyzed by TGA, elemental analysis, FTIR, UV–vis and XPS.

2.5. Computational details

Optimization calculations were performed using Gaussian 16 revision B.01 package at the DFT(M06-2X/Def2-TZVP) level of theory in the gas phase [26]. Harmonic frequency analysis has been systematically carried out to provide the absence of local minima or imaginary frequencies. Research of the ensemble of conformers of Rose Bengal over modified silica has been performed with the submodule CREST of XTB program [27,28]. Multiwfn software was used for quantitative analysis of molecular electron density isosurface, calculation of the extrema of the electrostatic potential [29,30] and evaluation of the overall surface area of Rose Bengal in condensed phase [31]. Atom in Molecules (AIM) analysis has been performed using the same program to provide the bond critical points (BCP) associated with the molecular interactions (electrostatic interactions and hydrogen bonding) in the case of the Rose Bengal and modified silica nanoparticles with ammonium moieties. These BCP have been characterized with different real-space functions:

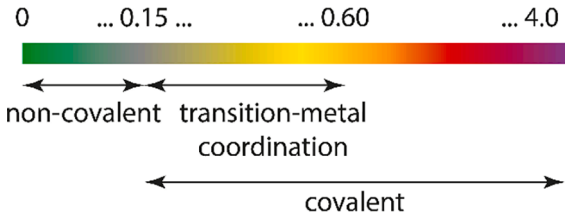
- The electron density ρ at the BCP for which a low-value (generally below 0.1 a.u.) indicates a non-covalent interaction.
- The laplacian of the electron density $\nabla^2\rho$ at the BCP whose a positive sign indicates a non-covalent interaction.
- The ratio between absolute value of potential energy V and lagrangian kinetic energy G, *i.e.* $|V|/G$ at the BCP, for which a value below 1.0 signals a closed-shell interaction, a value above 2.0, a covalent interaction [32].
- The ellipticity of the electron density at the BCP ε corresponding to the expression $(\lambda_1/\lambda_3) - 1$, with $\lambda_{1;3}$ the curvature of electron density perpendicular to the considered bond described by a BCP. A value equals to 0.0 indicates a symmetrical distribution of the electron density in the plane perpendicular to the bond. The larger this value deviates from 0.0, the more the electron density has an unsymmetrical distribution in this perpendicular plane, likely to reveal a non-covalent interaction.

NBO 7.0 program was employed to quantify donor-acceptor interactions (electrostatic and hydrogen-bonding) via the second order perturbation theory analysis [33]. The donor-acceptor transfer has also been depicted in the different tables. Intrinsic Bond Strength Index (IBSI) from the IGMPlot Software has also been used to reveal the strength and nature of each molecular interaction [34]. The expression of IBSI corresponds to:

$$\mathrm{IBSI} = \frac{d_{\mathrm{H_2}}^2}{d^2} \bullet \frac{\int \delta g^{\mathrm{pair}} \mathrm{d}\mathbf{r}}{\int \delta g^{\mathrm{H_2}} \mathrm{d}\mathbf{r}}$$

With d the distance between either the two hydrogens in H_2 molecule

or the two studied atoms and δg^{pair} the IGM descriptor between the two considered atoms explained further in the document. The typical scale of IBSI is given below:



IGMPlot has also been used to extract weak interactions between Rose Bengal and surface of silica nanoparticle with the δg^{inter} descriptor based on the gradient-based partition (GBP) [35,36]. This latter corresponds to the following expression:

$$\delta g^{inter} = \left|\nabla\rho^{IGM,\ inter}\right| - |\nabla\rho|$$

With,

$$\left|\nabla\rho^{IGM,\ inter}\right| = \sqrt{\left(\left(\frac{\partial\rho}{\partial x}\right)^{IGM,inter}\right)^2 + \left(\left(\frac{\partial\rho}{\partial y}\right)^{IGM,inter}\right)^2 + \left(\left(\frac{\partial\rho}{\partial z}\right)^{IGM,inter}\right)^2}$$

And,

$$\left(\frac{\partial\rho}{\partial\mu}\right)^{IGM,inter} = \left|\sum_{a=1}^{A}\frac{\partial\rho_a}{\partial\mu}\right| + \left|\sum_{b=1}^{B}\frac{\partial\rho_b}{\partial\mu}\right| (\mu = x,\ y \text{ or } z)$$

A and *B* being the two user-defined fragments with *a* and *b* the primitives associated to the atoms in the fragment *A* and the fragment *B* respectively. When A and B are two atoms, the descriptor is written δg^{pair} instead of δg^{inter}. $|\nabla\rho|$ is the true electron density gradient:

$$|\nabla\rho| = \sqrt{\left(\frac{\partial\rho}{\partial x}\right)^2 + \left(\frac{\partial\rho}{\partial y}\right)^2 + \left(\frac{\partial\rho}{\partial z}\right)^2}$$

Energy Decomposition Analysis based on Natural Orbital for Chemical Valence (EDA-NOCV) has been performed via ORCA 4.2.1 program to obtain the interaction energy between Rose Bengal and the surface of the silica nanoparticle in the case of the presence and absence of the ammonium moieties [37]. VMD 1.9.3 [38] and IBOView were employed for graphical outputs.

2.6. Singlet oxygen quantum yield [39]

Singlet oxygen quantum yields of RB@NS, RB@CS and RB@U were determined in water by monitoring the decomposition of a $^1O_2$ trap (AVS = Anthracene-9,10-divinylsulfonate) on a time range extending from 0 to 15 min. Practically, a O_2 balloon was bubbled in the cuvette for 15 min containing AVS (Absorbance = ~1 at 397 nm) and the photosensitizer (Absorbance = ~0.05 at 530 nm). The cuvette was irradiated at 530 nm and at regular intervals, an absorption spectrum was taken. The decomposition of AVS was then determined by analyzing the absorption decay of AVS at 397 nm. This protocol was repeated three times for each heterogenized material. The reference used was pure RB for which a singlet oxygen quantum yield of 0.75 in water is known [40]. Singlet oxygen quantum yields were determined based on the following equation:

$\phi_{sam} = \phi_{ref}*[(m_{sam}/m_{ref})*(L_{ref}/L_{sam})]$ where ϕ_{sam} and ϕ_{ref} are $^1O_2$ quantum yields of RB@SiO_2 heterogenized photocatalysts and RB, respectively, m_{sam} and m_{ref} are slopes in the plots of ΔA at the photoabsorption maximum wavelength of AVS (397 nm) against photoirradiation time, and L_{sam} and L_{ref} are light harvesting efficiencies, which are given by $L = 1–10^{-A}$ ("A" is the absorbance at the photoirradiation wavelength).

2.7. Citronellol photooxidation [7]

The quantity of RB needed for the reaction equals 4.9 mg to 5 mol%. The quantities of solid materials to introduce in the medium were determined by considering the loadings determined by TGA for each material: 4.9/0.13 = 38 mg for RB@NS, 4.9/0.19 = 26 mg for RB@CS and 4.9/0.16 = 30 mg for RB@U (the partial degradation of RB was not taken into account). The heterogenized photocatalyst was added in a 50 mL round-bottom flask, followed by 20 mL of MeCN. The resulting suspension was sonicated for 15 min at power 3 on a VWR ultrasonic bath. Citronellol (0.1 mmol, 1 eq., 15 mg, 18 µl) was added and O_2 was bubbled in the mixture. The medium was stirred and illuminated with green LEDs for 24 h. PPh_3 (0.12 mmol, 1.2 eq., 30.2 mg) was added and the mixture was stirred for 5 min. The solvent was evaporated under high vacuum, DCM was added and the medium was cooled to 0 °C for 15 min. Filtration on a PVDF Millipore Membrane (0.1 µm) allowed the recovery of the solid. The pink powder was washed with 3X25 mL of DCM. The resulting powder was finally dried under vacuum. The filtrate was recovered and the solvent was evaporated. Dimethylsulfoxide (DMS) was added to allow quantitative NMR analysis.

The recycling runs were conducted as explained above, except that for each run, the recovered materials were weighted again to ensure the same quantity of photocatalyst and if not, this quantity was corrected by adding materials from after the first run (but not fresh heterogenized photocatalyst as this would too strongly influence the results). The added amount was never more than 10% of the total. This has been only necessary for run 3.

3. Results and discussion

Nanospheres (40 nm) were synthesized according to the famous Stöber sol-gel process [6]. Core-Shell (core = 27 nm, mesoporous layer thickness = 15 nm, total size = 57 nm as measured by TEM) were obtained by adapting the procedure from Yoon *et al* [8]. U NPs were purchased from Strem (40–50 nm). The various architectures were confirmed by TEM microscopy (Fig. 1). XPS (Figs. S1, S4, S7) and IR (Figs. S3, S6, S9) analyses showed that the 3D inorganic network of SiO_2 was correctly formed and that no impurity was present, except for a small amount of unreacted TEOS seen by XPS and FTIR- peaks at 1633 and 948 cm^{-1}. The specific surface areas were calculated by using the BET equation on nitrogen physisorption data: NS = 360 m^2/g; CS = 650 m^2/g; U = 243 m^2/g (Figs. S2, S5, S8). These values are within the expected scale as core-shell NPs were the only mesoporous material. Urchins nanoparticles were expected to be more porous. These three materials present a weakly acidic surface due to the presence of silanol groups with a density generally comprised between 4 and 6 Si–OH/nm^2. A lower density of 1.5–2.5 SiOH/nm^2 is expected for high-temperature calcinated silica nanoparticles that can be improved followed rehydration [41]. The surface chemistry of silica nanoparticles also governs its hydrophilic/hydrophobic character, that depends on the ability of Si–OH groups to form hydrogen bonds with an adsorbate [42] and on the surface roughness [43]. Sriramulu *et al.* were able to prepare a thin film of unfunctionalized non-porous silica nanoparticles and showed their superhydrophilic character by measuring a water contact angle of 0° [44]. Mesoporous silica nanoparticles are also hydrophilic with reported water contact angles of 30° and 0° for MCM-48 and MCM-41, respectively [43,45]. Pristine dendritic mesoporous silica nanoparticles are also known to be hydrophilic materials. A lot of researches focused on increasing their hydrophobicity by implementing alkyl moieties or by applying treatments to remove the silanol groups [46–48].

In order to immobilize RB non-covalently, a general 3-step functionalization method was envisaged (Scheme 2). The first step was the anchoring of tertiary amines by using of (*N*,*N*-dimethylaminopropyl) trimethoxysilane (DAPTMS) in toluene under reflux for 24 h [24]. The second step was the methylation of previously anchored amines with

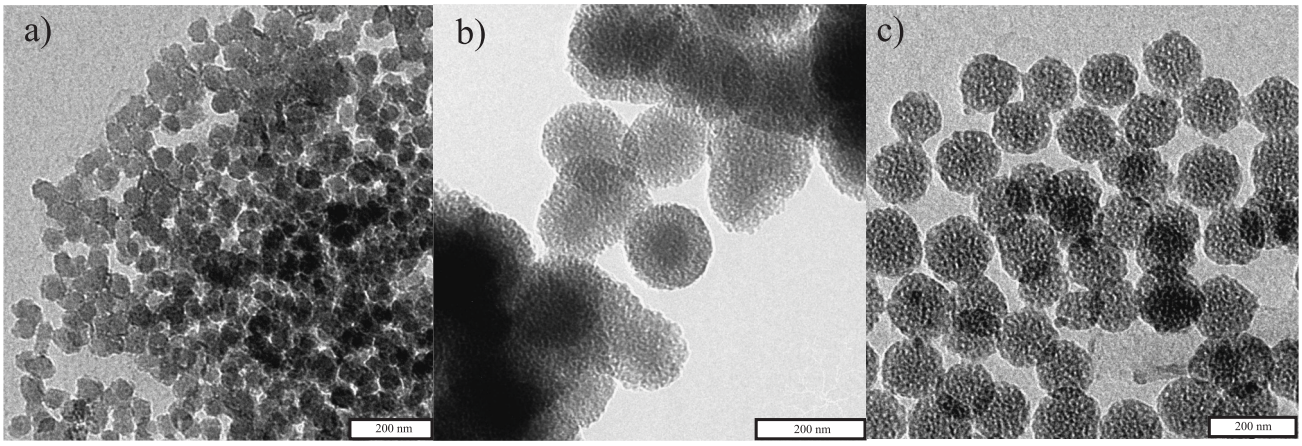
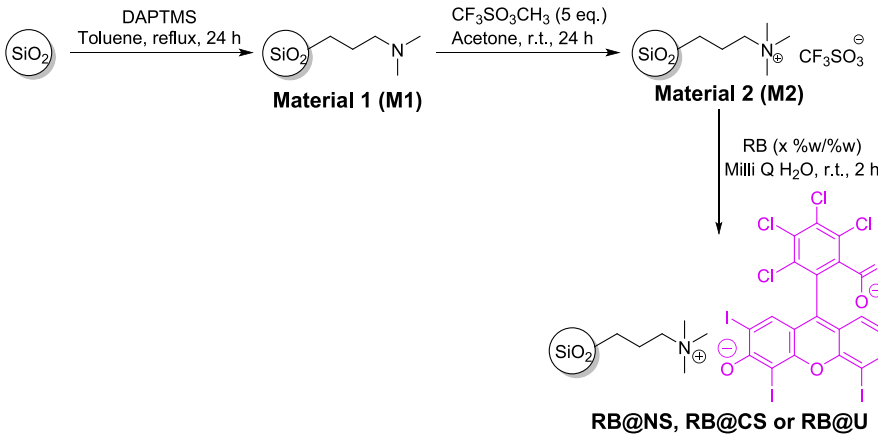


Fig. 1. TEM images of pristine silica NPs: a) NS, b) CS, c) U.



Scheme 2. The three-step functionalization method envisaged to immobilize RB.

$CF_3SO_3CH_3$ to obtain ammonium moieties [25]. The last step was the immobilization of RB *via* electrostatic interactions by contacting RB with the functionalized support in water.

The heterogenized photocatalysts (RB@NS, RB@CS and RB@U) and the intermediate materials (materials 1 and 2) for each nanostructured support were characterized by XPS, CHN and TGA analyses and the values are reported in Table 1.

For material 1, the detection of a nitrogen peak with a 399.6 eV binding energy by XPS proved the efficient anchoring of tertiary amine moieties for the three silica morphologies (Fig. S10) [49]. The N/Si ratio permits to compare the efficiency of amines anchoring among the three different morphologies. As XPS is a surface analysis, the first few

Table 1
Characterization of the heterogenized photocatalyst and the intermediate materials by XPS, CHN and TGA analyses. *wt.% of N was calculated based on TGA curves. Nitrogen content represents 16.3 % of the organic part, multiplying that value by the loss in weight assessed by TGA leads to the evaluated quantity of nitrogen (S12).

	NS			CS			U			Pure RB-
	M1	M2	RB@NS	M1	M2	RB@CS	M1	M2	RB@U	
XPS (atomic%)										
C_{1s}	20.8	17.2	24.7	19.0	17.1	26.1	15.5	15.6	19.1	60.2
O_{1s}	57.1	50.1	45.5	58.1	50.9	48.9	61.9	49	45.4	9.3
Si_{2p}	18.5	19.4	23.2	19.3	18.5	18.5	19.5	25.1	20.4	–
N_{1s}	3.6	2.8	2.1	3.5	2.7	2.2	3.1	2.2	1.9	–
F_{1s}	–	8.4	Traces	–	8.5	Traces	–	7.2	Traces	
S_{2p}	–	2.2	–	–	2.3	–	–	2.0	–	–
I_{3d}	–	–	1.8	–	–	2.2	–	–	3.4	10.5
Cl_{2p}	–	–	2.4	–	–	2.2	–	–	3.1	12.2
Na_{1s}	–	–	0.3	–	–	0.2	–	–	0.7	7.8
O/Si	2.1	2.5	2.0	2.4	2.7	2.6	2.7	2.0	2.0	–
N/Si	0.2	0.1	0.1	0.2	0.2	0.1	0.1	0.1	0.1	–
I/Cl	–	–	0.7	–	–	1	–	–	1.1	0.9
NMe_3^+/Cl	–	–	1.6	–	–	1.6	–	–	1.5	–
CHN (wt.%)										
N	–	1.02	0.90	–	1.44	0.98	–	0.87	0.62	–
TGA (wt.%)										
N*	2.62	1.31	–	2.18	1.46	–	1.47	0.84	–	–

nanometers (5–10 nm) of the material will be analyzed and the core of the particles will not. This feature means that for porous materials, some functionalities will not be detected because they are too deep while for non-porous materials, all functionalities will be detected (Fig. 2). The consequence is that the N/Si ratio is overestimated for NS and slightly underestimated for CS and U NPs, meaning that CS seems to present the best functionalization rate. Another parameter that can influence the surface atomic concentration in nitrogen is the ability of multi(tri)-valent silane (such as DAPTMS) to form infinite, cross-linked siloxane polymer lattices. This phenomenon is well known in literature [24,50] and lead to multiple layer of DAPTMS with some nitrogen moieties that are not easily accessible for further functionalization steps. This first step was also confirmed by TGA analysis for which an important loss in mass was observed for NS although this nanostructure is not porous. We could envisage that for this architecture, the DAPTMS polymerization was favored.

The second step was the formation of ammonium moieties, leading to material 2 [25]. This functionalization step was also evaluated by XPS analyses (Figs. S12–S14). In all three cases, a N_{1s} peak was observed at around 402 eV corresponding to quaternary amines [49]. Some tertiary amines were still detected at 399.6 eV (7.5 % for NS, 4.7 % for CS and 5.8 % for U of the N_{1s} peak). The higher amount of tertiary amines for NS reinforce the DAPTMS polymerization hypothesis for which nitrogen elements could be buried and not able to be transformed into positively charged moieties. The presence of ammonium functions was also supported by the detection of fluorine and sulfur elements, forming the counter anion (Table S1).

As the XPS depth of analysis limitation, as discussed above, prevents the quantification, CHN and TGA analyses were performed for the three solids (Table 1, Fig. S15). For TGA analyses, the hypotheses are that the loss in weight is due only to perfectly anchored ammonium arms (no impurity) and that the organic arms are completely calcinated during the TGA analysis. For all supports, TGA and CHN analyses were in agreement, except for NS particles for which a slightly higher amount in nitrogen was assessed by TGA (S12). CS showed the higher level of functionalization while U showed the worst, as expected from their specific surface areas.

FTIR provided further evidence for the anchoring of ammonium moieties. Comparing the spectra of NPs-NMe_3^+ with that of pristine NPs on Figs. S20–S22, the presence of characteristic stretching bands of ammonium moieties (1630 and 1490 cm^{-1}) and, more importantly, of CF_3SO_3 (640 cm^{-1}) validated the successful introduction of desired functionality at the surface of NPs.

The next step was the immobilization of RB to give heterogenized photocatalysts noted RB@NS, RB@CS and RB@U (Scheme 2). The hydrophilic head of ammonium-functionalized silica nanoparticles allowed an efficient dispersion of the materials in water in all three cases, indicating that the hydrophilicity of silica nanoparticles was maintained (Fig. S24). The maximal loading of RB was determined by varying the %w/w of RB introduced with silica in several experiments and the resulting bright pink solids were analyzed by TGA while the filtrates were analyzed by UV–vis. M.A. Rauf *et al.* were able to determine experimentally the dipolar moment of Rose Bengal in its fundamental and excited states, namely 1.72 and 2.33 Debye, respectively [51]. This is a small change and if we consider only electrostatic interactions, it would mean that the adsorption of RB would be slightly enhanced when performed in its excited state. We can consider that the difference in Rose Bengal adsorption whether it is performed in the dark or under light is not significant. The most porous structure, CS, gave the highest loading of 19 wt.% followed by U (15 wt.%) and NS (13 wt.%). Although NS and U presented the lowest loadings, it was still quite high compared with CS and taking into account their respective specific surface areas. The heterogenized photocatalysts were analyzed by IR, CHN, XPS and UV–vis to confirm that the structure of RB and its photoactivity were intact after immobilization.

The FTIR spectra of NPs-RB suggested the incorporation of the intact dye onto the materials. Indeed, the characteristic bands of RB observed for the free molecule at 1614, 1543, 1446 and 1340 cm^{-1} (Fig. S18) have been identified after immobilization at 1614, 1548, 1457 and 1342 cm^{-1} (Figs. S20–S22) in all three cases.

The heterogenized photocatalysts were also analyzed by XPS. The first thing to check was the stability of our functionalized arms. Ammoniums moieties were still detected but with a lower amount than before the immobilization of RB (Table 1). This phenomenon was confirmed by CHN analyses (Table 1) and could be explained by the basicity of the photocatalyst that could induce a Hoffman elimination or by the alkylation of RB. However, some CF_3 moieties were still detected by XPS.

The second important information is the detection of chlorine and iodine, which are characteristic elements of the photocatalyst. These elements were spotted by XPS at the same binding energy as the pure powder of RB (Fig. S16) and the atomic concentration ratio I/Cl fitted also to the reference. When analyzing the pure powder of RB, decomposition of the I_{3d} photopeak gave two components: one at 620.6 eV corresponding to I-C bond and the other one at 618.5 eV for 5 % of the amount of iodine corresponding to I^-. It cannot be excluded that the XPS analysis itself causes the breaking of I-C bonds. On the supports, this 618.5 eV component increased to 35 % for CS, 26 % on U, while for NS, this value reached 55 % of the total amount of iodine (Fig. 3).

In addition, the detection of sodium (the counter-ion of RB at the start) on the surface indicates the occurrence of a non-specific physical adsorption of RB, rather than ion-exchange at the ammonium-sites, that cannot be avoided for each material. This non-specific interaction was three times more important on U NPs (Na/Si = 0.03) than on NS and CS nanostructures. A computational study was carried out to assess the energy of interaction between RB and the surface of the modified silica NPs with ammonium moieties and between RB and silica NPs without any ammonium functionalities at the surface and these energies are −74.25 and −46.64 kcal/mol, respectively (S19-S30). This proves the utility of functionalizing the surface of NPs to enhance the immobilization rate of RB. This adsorption phenomenon was also confirmed experimentally by putting in contact pristine NS (as it possesses the

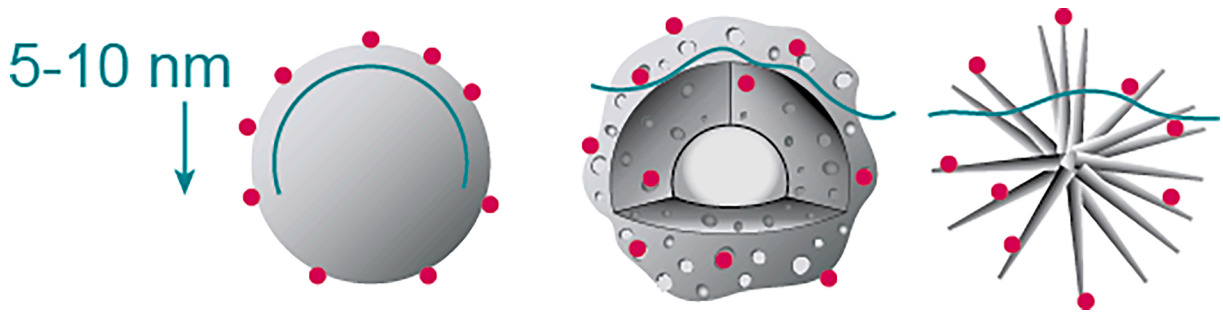


Fig. 2. XPS depth of analysis sketched for each silica morphology leading to an over- or underestimation of functionalization rate. The limit in the depth of analysis is marked by the green line, while pink balls represent some anchored heteroatoms.

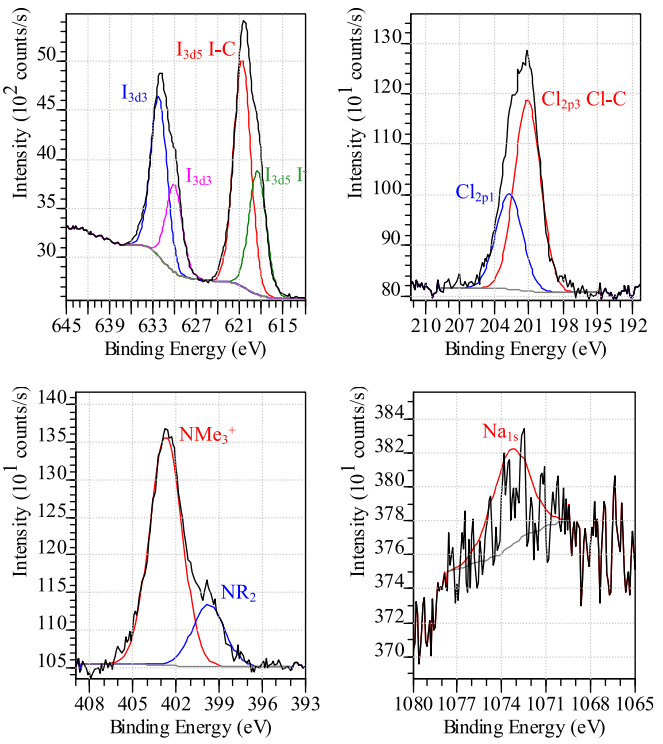


Fig. 3. I_{3d}, Cl_{2p}, N_{1s} and Na_{1s} XPS spectra of immobilized RB onto CS structures.

lowest specific surface area) with RB. A loading of 3 wt.% and 4.7 wt.% of RB was measured by UV–vis and TGA, respectively which is much lower than the loadings obtained on ammonium-functionalized NPs.

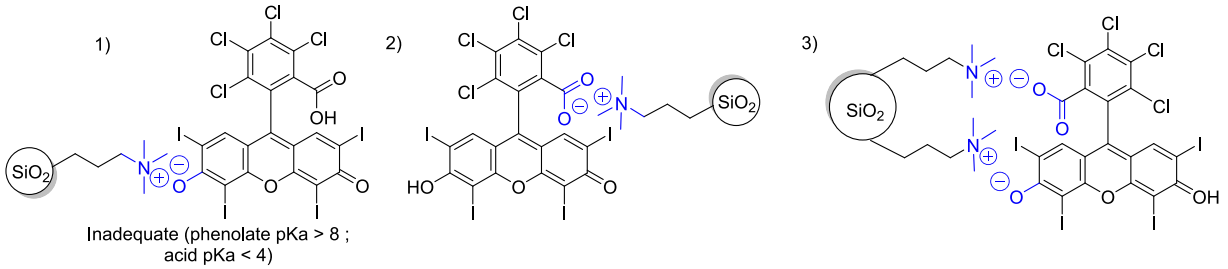
Finally, the NMe_3^+/Cl ratio gave us an idea about how the interaction between RB and the support was realized. If one anionic site of RB was involved in the immobilization, two situations were possible: the electrostatic interaction with the phenolate or with the carboxylate. The first one was inadequate in terms of pKa and, furthermore, a computational study had been carried out, revealing that the second interaction with the carboxylate was the most favored (Scheme 3). As the NMe_3^+/Cl ratio ranged from 1.6 to 1.8 for the three supports, the situation where the two anionic sites of RB interact with two distinct ammonium groups needed to be considered. This information given by XPS was supported by TGA from which the ammonium density was calculated. Considering the interacting sphere of one RB molecule with silica NPs modified surface, 2.96, 2.31 and 3.74 ammoniums were available to immobilize one molecule of the dye for NS, CS and U, respectively (see S12) leading to a possible double-side interaction. This ammonium density explains the detection of free $CF_3SO_3^-$ moieties by XPS for heterogenized photocatalysts (being the counter anion of ammonium groups) as an excess of these moieties were present at the surface. Moreover, this double-side interaction was interesting as it prevented RB from being too easily released in the mobile phase and also protected it from photobleaching as it was observed by Terra *et al.* [52] Furthermore, this double-sided interaction diminishes the free ammonium moieties at the surface leading to a decrease in the hydrophilicity of the silica nanoparticles, which is necessary for their correct dispersion in acetonitrile used as solvent in the photooxidation of citronellol.

Although the results converge to a double-side interaction, we needed to confirm that it was structurally feasible by considering the two perpendicular planes of the RB molecule. Again, a computational study was carried out by implementing the density of ammonium functionalized arms and we could clearly see that two separated ammonium arms can indeed interact with the anionic sites of RB *via* electrostatic interactions revealed by the Independent Gradient Model methodology (Fig. 4) [35,36]. Some hydrogen bonds were also visualized, reinforcing the interaction with the support.

Photophysical properties of RB@NPs were evaluated by UV–vis spectroscopy (Table 2). For supported RB, a slight bathochromic shift of the absorbance peak was observed in comparison to RB in acetonitrile (Fig. S23). According to the literature, this red shift can be ascribed to the chemical and polarity environment modification of RB [40]. Heterogenized photocatalyst showed also a decrease in ε due to the presence of solid nanoparticles causing light diffusion. RB@CS showed the best photophysical properties in terms of ε and photostability (ΔA) and its ability to produce $^1O_2$ was equivalent to pure RB. Strikingly, the presence of the supports enhances the RB photostability [52,53]. Finally, RB@NS had the highest quantum yield of production of $^1O_2$ of 0.94. The direct surface accessibility for light could be an advantage as this silica is non-porous. Surprisingly, RB@U didn't show the best photophysical properties as we would have expected thanks to the multiple scattering events increasing the light path between neighbouring molecules anchored within the spikes of the urchins [54].

To benchmark the reactivity of these immobilized photocatalysts, the materials were tested on the photooxidation of citronellol [7], for which RB in homogeneous phase is known to be effective (Scheme 4), and which requires singlet oxygen. Control experiments showed that with no light, or no photocatalyst, only traces of products were observed. Using a photocatalyst loading of 5 mol%, pure RB gave a 94 % yield of the two regioisomers 2 and 3 (ratio 1.1/1) within an irradiation time of 2 h. RB@NS was the first heterogenized system to be used to optimize the reaction with the solid catalysts. With an increased irradiation time to 18 h (as the diffusion will be slowed down in presence of a solid), an NMR yield of 71 % and a ratio of 1:1 between products 2 and 3 were determined. By increasing the irradiation time to 24 h, a quantitative yield was obtained. These optimized conditions were used with RB@CS and RB@U and quantitative NMR yields were also obtained, with the same regioisomers ratio.

Recycling runs were then conducted under the same conditions for all supports. The NMR yield with NS dropped by half at the second run, and could be increased again by increasing the catalyst amount in the third run, to counterbalance any recovery losses. RB@NS subsequently presented a stable NMR yield of 66 %. Concerning the urchins, the commercial support, a quantitative yield was observed for the first two runs before decreasing and reaching about 50 % for the fourth and fifth runs. The last material, RB@CS, was revealed to be the most efficient



Scheme 3. Three different ways to immobilize RB onto the surface of silica NPs.

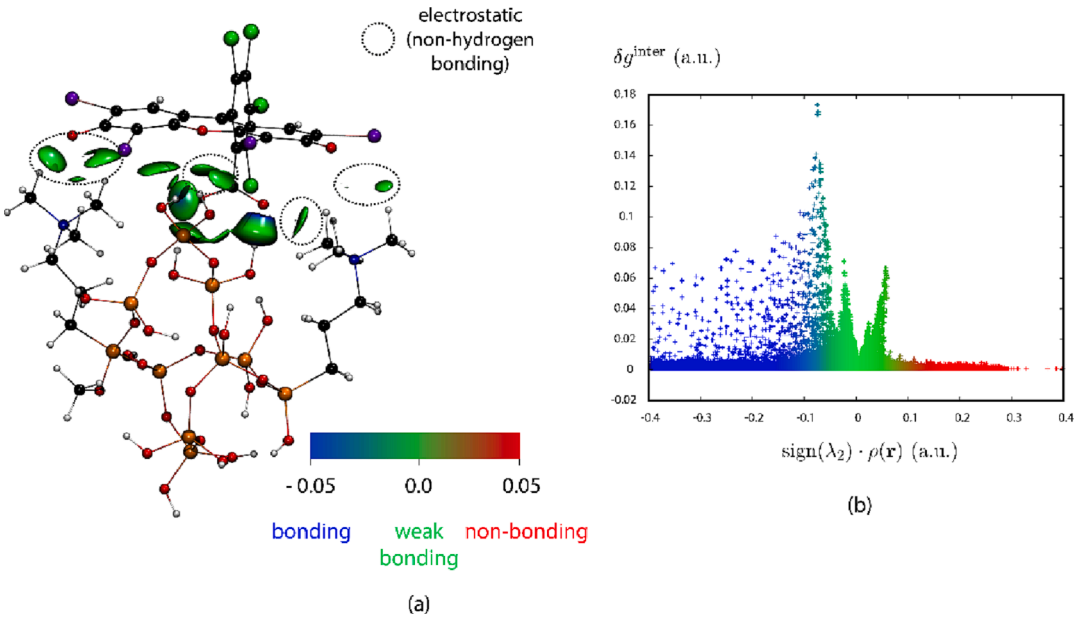
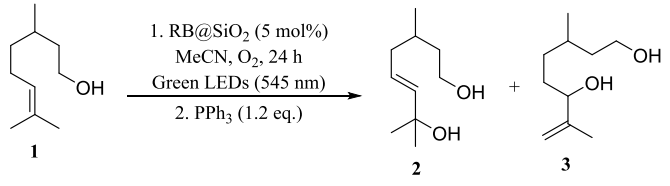


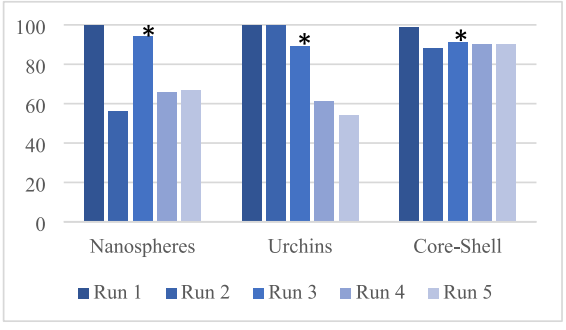
Fig. 4. Computational study of the double-side interaction between RB and the ammonium groups anchored at the surface of NPs along with hydrogen bonding. White = H, Black = C, Red = O, Brown = Si, Blue = N, Purple = I and Green = Cl. Electrostatic interactions (non-hydrogen bonding) are indicated by dotted black circles in (a). Blue-Green-Red (BGR) color range for the value of sign(λ_2)·ρ(**r**) (λ_2 standing for the second eigenvalue of the hessian matrix of electron density) is given with δg^{inter} = 0.05 a.u. in (a) and in the signature of molecular interactions in (b). Level of theory: M06-2X/Def2-TZVP. (For interpretation of the references to color in this figure legend, the reader is referred to the web version of this article.)

Table 2
Photophysical properties of RB and supported RB.

	RB	RB@NS	RB@CS	RB@U
λ_{max} (nm)	557	562	562	562
ε ($mol^{-1}.cm^{-1}$)[a]	72.800	15.000	19.300	15.000
ϕ_Δ[b]	0.75	0.94	0.74	0.64
ΔA[c]	0.550	0.034	0.016	0.012

[a] ε were determined in acetonitrile. [b] ϕ_Δ was determined by AVS photodegradation in water (Figs. S29–S32) [39]. [c] ΔA was the decrease in absorbance of the photocatalyst after 15 min of irradiation.





Scheme 4. NMR yields (regioisomers 2 and 3) of photooxidation of citronellol. The internal standard used was dimethylsulfone (Scheme S2). *In all cases, to conduct run 3, some material arising from run 1 was added to insure same catalyst total mass.

immobilized photocatalyst, as expected as it showed the best photophysical properties (Table 2). A quantitative yield was obtained in the first run and the photoactivity of RB was stabilized along five runs (NMR yield in the 5th run = 90 %).

For each run, an evaluation of the RB leaching was realised by UV–vis analysis of the filtrates and TGA of the solids (Table S5). This leaching could occur by simple loss of RB or loss of ammonium arms. The leaching calculated by TGA after the first run was important for RB@NS (4.91 %) and RB@U (6.74 %), explaining in part the decrease in photoactivity in the next runs. The RB leaching evaluated by UV–vis gave the same scale for the three different morphologies: 2.75, 2.63 and 8.50 wt.% for RB@NS, RB@CS and RB@U, respectively. Although, a moderate value was obtained for NS NPs comparing to the value obtained by TGA, meaning that the ammonium arms could possibly suffer from light irradiation and stirring.

At this stage, the leaching could be explained by the loss of RB that was weakly immobilized onto silica such as the one that was non-specifically adsorbed (as already discussed above) or the one that was involved in π-π stacking forming multiple layers thanks to the aromatic nature of RB. To validate this last hypothesis, the amount of RB necessary to form a monolayer was calculated and compared with the quantity of RB introduced. Knowing the ammonium densities and the overall surface area of RB, we could determine that $7.40E^{18}$, $1.34E^{19}$ and $5.01E^{18}$ RB entities were needed to form a monolayer of RB at the surface of the nanoparticles. By comparing these values to the amount of RB immobilized on the supports, the excesses of RB were determined and validated the possibility of having π-π stacking: $5.24E^{17}$, $3.08E^{16}$, $7.77E^{18}$ for NS, CS and U, respectively (see S34). The excesses were quite high for RB@NS and RB@U explaining the leaching of RB during the first run for those supports. Moreover, the important leaching for RB@U was understood as the non-specific adsorption phenomenon was also important on that support. This π-π stacking was also a key information to understand the high loadings in RB for all 3 materials that were obtained compared to what we expected considering the specific surface areas of the different morphologies. Core-Shell structures seems to prevent that interaction as a slight excess of RB and a low leaching were observed.

For the following recycling runs, once the excess of RB was "removed", the photoactivity of RB@NS was stable along the runs while for RB@U, it kept dropping. RB@CS was efficient along the runs (Table S5).

To understand further the differences in photoactivity, final recycled materials were analysed. Firstly, their morphologies were investigated by TEM and no changes were observed. All nanostructures were unaltered under photoirradiation and stirring (Fig. S33).

Secondly, CHN and XPS analyses were performed to evaluate the robustness of the ammonium-functionalized arm and the chemical structure of RB, respectively. CHN analyses proved the stability of the functionalized arm for two materials as no loss of nitrogen was detected in the cases of CS (0.96 and 0.98 wt.% N) and U (0.62 and 0.68 wt.% N, before and after 5 runs of photooxidation, respectively). On the contrary, NS showed a slight decrease in nitrogen content from 0.89 to 0.74 wt.% N after 5 runs. Functionalization of simple silica spheres seemed to suffer from light and abrasion while the other architectures being porous and allowing internal functionalization acted as a shield for the anchored arms.

Concerning the photocatalyst, XPS analyses showed an important loss in iodine and chlorine elements. The ratio I/Cl was unbalanced, explained by the accentuated loss in iodine (Table 3 and Fig. 5). The formation of iodide increased under light reaching 85 % of total iodine in all cases. Furthermore, the photobleaching of C-Cl bond occurred along the runs and chloride was detected up to 61 % of the total amount of chlorine while none was detected before photocatalytic runs. As the whole structure was not analysed by XPS in the case of U and CS because of the depth of analysis limitation, the RB buried deep in the pores could not be detected by XPS, so the extent of photobleaching was clearly overestimated. These known photobleaching phenomena [55–57] could also partially explain the decrease in photoactivity for RB@NS for which these photodegradations could happen more rapidly than for RB@CS and RB@U. The commercial support suffered from a high leaching explaining the decrease photoactivity. In Core-Shell structure, RB seemed to be protected for a longer time from photobleaching, as indicated by the photophysical characterization reported in Table 2. Finally, the expected absorption peak was still distinguishable in the absorption curves obtained by UV–vis analysis of the solids after 5 runs, in line with retained photoactivity (Fig. S34). All in all, this demonstrated the superiority of the core-shell structure and the ammonium immobilization strategy.

4. Conclusion

Rose Bengal was immobilized *via* electrostatic interactions onto three different morphologies of silica nanoparticles, namely Nanospheres (NS), Core-Shell (CS) and Urchins (U). The impact of these different architectures was studied on the production of singlet oxygen for application in citronellol photooxidation.

To allow the dye immobilization, a general three-steps methodology was used to functionalize the materials: the anchoring of tertiary amines followed by their methylation, leading to ammonium moieties that can immobilize RB by ion-exchange. For all supports, the presence of these positively charged groups was proven by XPS and IR. The immobilization of RB was successful, reaching the highest loading of 19 wt% on CS. The photophysical properties of immobilized RB were determined for each solid and CS particles were determined as the best support with photophysical properties similar to that of pure RB. The possibility of double ion interaction between the support and RB increased even further the robustness of our methodology, which allowed organic dye immobilization without any modification to the active molecule.

Table 3
XPS analysis of final materials after 5 runs of photooxidation. The values are expressed in atomic concentration percentage.

	C_{1s}	O_{1s}	Si_{2p}	N_{1s}	I_{3d}	Cl_{2p}	O/Si	I/Cl
NS	17.0	53.3	26.7	1.9	0.2	0.8	2.0	0.3
CS	23.6	50.4	23.1	1.6	0.2	0.7	2.2	0.3
U	23.0	50.0	24.6	1.8	0.3	0.7	2.0	0.4

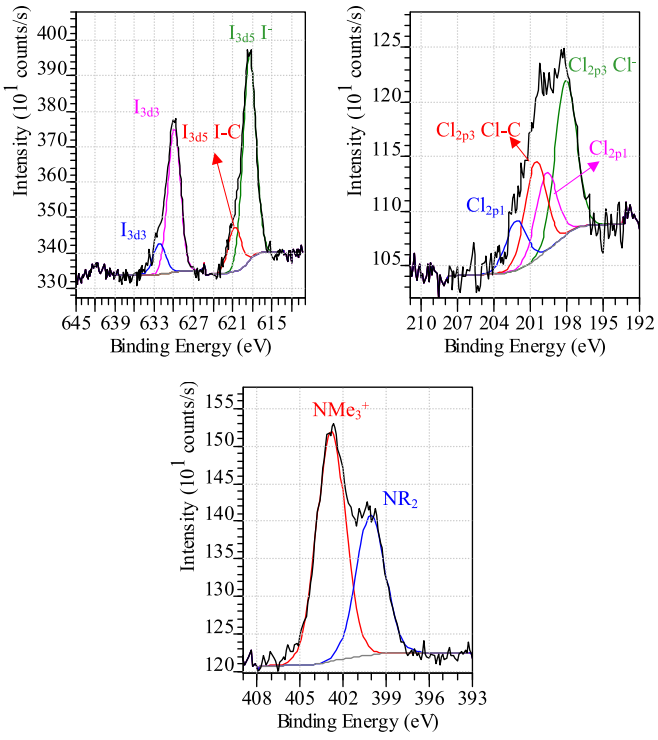


Fig. 5. I_{3d}, Cl_{2p} and N_{1s} XPS spectra of immobilized RB onto CS structures after five catalytic runs.

The citronellol photooxidation was used as benchmark reaction to test the efficiency of the heterogenized photocatalysts. All immobilized photosensitizers were active and could be recycled at least 5 times. XPS analyses demonstrated the occurrence of a photobleaching on all supports (breaking of C-Cl and C-I bonds) but the activity was maintained. RB@NS and RB@U suffered from leaching explaining the decrease in photoactivity, reaching 65 and 53 % NMR yield in the fifth run, respectively. Moreover RB@NS showed a decrease in nitrogen content *via* CHN analysis, indicating that some ammoniums moieties were also lost, due to the non-porous nature of this support and the presence of functional groups at the external surface rendering them more fragile. The best results were obtained with RB@CS, in which case the leaching was moderate thanks to limited π-π stacking multi-layer interactions, giving an average 90% NMR yield throughout the five runs.

In conclusion, there is a clear influence of the architecture of silica nanoparticles onto the production of singlet oxygen by immobilized RB. The Core-Shell morphology seemed to be the best choice in terms of photophysical properties, activity and recycling of the surface-bound molecule. Although some photobleaching was detected at the surface for this material, we could hypothesize that the porous structure acts as a shield and protects RB in the pores explaining its high photoactivity along the five runs.

CRediT authorship contribution statement

Nathalie Body: Writing – original draft, Methodology, Investigation, Conceptualization. **Corentin Lefebvre:** Writing – review & editing, Investigation, Data curation. **Pierre Eloy:** Formal analysis, Data curation. **Tommy Haynes:** Formal analysis, Data curation. **Sophie Hermans:** Writing – review & editing, Supervision, Funding acquisition, Conceptualization. **Olivier Riant:** Writing – review & editing, Supervision, Funding acquisition, Conceptualization.

Declaration of Competing Interest

The authors declare that they have no known competing financial interests or personal relationships that could have appeared to influence the work reported in this paper.

Data availability

Data will be made available on request.

Acknowledgements

NB and SH thank the Belgian National Funds for Scientific Research (F.R.S.-FNRS) for their Fund for Research Training in Industry and Agriculture (FRIA) PhD grant and Research Director position, respectively. NB thanks also Région Wallonne for its participation in the FRIA scheme. The authors thank Jean-François Statsyns and Fabio Lucaccioni for BET measurements and CHN analyses, respectively. They also thank Dr. S. Ouk for his generous financial support through the Fondation Louvain allowing the purchase of a solvents purification system.

Appendix A. Supplementary data

Supplementary data to this article can be found online at https://doi.org/10.1016/j.jphotochem.2023.114648.

References

[1] C.S. Foote, S. Wexler, Olefin oxidations with excited singlet molecular oxygen, J. Am. Chem. Soc. 86 (18) (1964) 3879–3880.
[2] C.S. Foote, S. Wexler, Singlet oxygen. A probable intermediate in photosensitized autoxidations, J. Am. Chem. Soc. 86 (18) (1964) 3880–3881.
[3] I. Pibiri, S. Buscemi, A. Palumbo Piccionello, A. Pace, Photochemically produced singlet oxygen: applications and perspectives, ChemPhotoChem. 2 (2018) 535–547.
[4] M.C. DeRosa, R.J. Crutchley, Photosensitized singlet oxygen and its applications, Coord. Chem. Rev. 233-234 (2002) 351–371.
[5] L. Wang, U.S. Schubert, S. Hoeppener, Surface chemical reactions on self-assembled silane based monolayers, Chem. Soc. Rev. 50 (11) (2021) 6507–6540.
[6] W. Stöber, A. Fink, E. Bohn, Controlled growth of monodisperse silica spheres in the micron size range, J. Colloid Interface Sci. 26 (1) (1968) 62–69.
[7] J.C.S. Terra, A. Desgranges, C. Monnereau, E.H. Sanchez, J.A. De Toro, Z. Amara, A. Moores, Photocatalysis meets magnetism: designing magnetically recoverable supports for visible-light photocatalysis, ACS Appl. Mater. Interfaces 12 (2020) 24895–24904.
[8] S.B. Yoon, J.-Y. Kim, J.H. Kim, Y.J. Park, K.R. Yoon, S.-K. Park, J.-S. Yu, Synthesis of monodisperse spherical silica particles with solid core and mesoporous shell: mesopore channels perpendicular to the surface, J. Mater. Chem. 17 (2007) 1758–1761.
[9] T. Haynes, O. Bougnouch, V. Dubois, S. Hermans, Preparation of mesoporous silica nanocapsules with a high specific surface area by hard and soft dual templating approach: Application to biomass valorization catalysis, Micropor. Mesopor. Mater. 306 (2020) 110400.
[10] A. Maity, V. Polshettiwar, Dendritic fibrous nanosilica for catalysis, energy harvesting, carbon dioxide mitigation, drug delivery, and sensing, ChemSusChem 10 (20) (2017) 3866–3913.
[11] L. Liu, H. Liu, Y.-P. Zhao, Y. Wang, Y. Duan, G. Gao, M. Ge, W. Chen, Directed synthesis of hierarchical nanostructured TiO2 catalysts and their morphology-dependent photocatalysis for phenol degradation, Environ. Sci. Tech. 42 (7) (2008) 2342–2348.
[12] Y. Yu, P. Zhang, L. Guo, Z. Chen, Q. Wu, Y. Ding, W. Zheng, Y. Cao, The design of TiO2 nanostructures (nanoparticle, nanotube, and nanosheet) and their photocatalytic activity, J. Phys. Chem. C 118 (24) (2014) 12727–12733.
[13] A.N. Banerjee, The design, fabrication, and photocatalytic utility of nanostructured semiconductors: focus on TiO2-based nanostructures, Nanotechnol. Sci. Appl. 4 (2011) 35–65.
[14] J.G. Mahy, L. Lejeune, T. Haynes, N. Body, S. De Kreijger, B. Elias, R.H.M. Marcilli, C.-A. Fustin, S. Hermans, Crystalline ZnO Photocatalysts Prepared at Ambient Temperature: Influence of Morphology on p-Nitrophenol Degradation in Water, Catalysts 11 (2021) 1182.
[15] A. Mclaren, T. Valdes-Solis, G. Li, S.C. Tsang, Shape and size effects of ZnO nanocrystals on photocatalytic activity, J. Am. Chem. Soc. 131 (35) (2009) 12540–12541.
[16] A. Maldotti, A. Molinari, G. Varani, M. Lenarda, L. Storaro, F. Bigi, R. Maggi, A. Mazzacani, G. Sartori, Immobilization of (n-Bu4N) 4W10O32 on mesoporous MCM-41 and amorphous silicas for photocatalytic oxidation of cycloalkanes with molecular oxygen, J. Catal. 209 (1) (2002) 210–216.
[17] D. González-Muñoz, A. Gómez-Avilés, C.B. Molina, J. Bedia, C. Belver, J. Alemán, S. Cabrera, Anchoring of 10-phenylphenothiazine to mesoporous silica materials: A water compatible organic photocatalyst for the degradation of pollutants, J. Mater. Sci. Technol. 103 (2022) 134–143.
[18] D. González-Muñoz, A. Casado-Sánchez, I. del Hierro, S. Gómez-Ruiz, S. Cabrera, J. Alemán, Size-selective mesoporous silica-based Pt (II) complex as efficient and reusable photocatalytic material, J. Catal. 373 (2019) 374–383.
[19] K. Mori, M. Tottori, K. Watanabe, M. Che, H. Yamashita, Photoinduced aerobic oxidation driven by phosphorescence Ir (III) complex anchored to mesoporous silica, J. Phys. Chem. C 115 (43) (2011) 21358–21362.
[20] Y. Guo, S. Rogelj, P. Zhang, Rose Bengal-decorated silica nanoparticles as photosensitizers for inactivation of gram-positive bacteria, Nanotechnology 21 (2010), 065102.
[21] A. Uppal, B. Jain, P.K. Gupta, K. Das, Photodynamic action of Rose Bengal silica nanoparticle complex on breast and oral cancer cell lines, Photochem. Photobiol. 87 (2011) 1146–1151.
[22] E. Gianotti, B. MartinsEstevão, F. Cucinotta, N. Hioka, M. Rizzi, F. Renò, L. Marchese, An efficient rose bengal based nanoplatform for photodynamic therapy, Chemistry–A Eur. J. 20 (35) (2014) 10921–10925.
[23] S.M. Soria-Castro, B. Lebeau, M. Cormier, S. Neunlist, T.J. Daou, J. Goddard, Organic/Inorganic Heterogeneous Silica-Based Photoredox Catalyst for Aza-Henry Reactions, Eur. J. Org. Chem. 2020 (2020) 1572–1578.
[24] R.G. Acres, A.V. Ellis, J. Alvino, C.E. Lenahan, D.A. Khodakov, G.F. Metha, G. G. Andersson, Molecular structure of 3-aminopropyltriethoxysilane layers formed on silanol-terminated silicon surfaces, J. Phys. Chem. C 116 (10) (2012) 6289–6297.
[25] D. Vidick, M. Herlitschke, C. Poleunis, A. Delcorte, R.P. Hermann, M. Devillers, S. Hermans, Comparison of functionalized carbon nanofibers and multi-walled carbon nanotubes as supports for Fe–Co nanoparticles, J. Mater. Chem. A 1 (6) (2013) 2050–2063.
[26] M.J. Frisch, G.W. Trucks, H.B. Schlegel, G.E. Scuseria, M.A. Robb, J.R. Cheeseman, G. Scalmani, V. Barone, G.A. Petersson, H. Nakatsuji et al., Gaussian 16, Revision B.01, Gaussian, Inc., Wallingford CT, 2016.
[27] C. Bannwarth, E. Caldeweyher, S. Ehlert, A. Hansen, P. Pracht, J. Seibert, S. Spicher, S. Grimme, Extended tight-binding quantum chemistry methods, Wiley Interdisciplinary Reviews: Computational Molecular, Science 11 (2021) e1493.
[28] P. Pracht, F. Bohle, S. Grimme, Automated exploration of the low-energy chemical space with fast quantum chemical methods, PCCP 22 (14) (2020) 7169–7192.
[29] T. Lu, F. Chen, Multiwfn: a multifunctional wavefunction analyzer, J. Comput. Chem. 33 (2012) 580–592.
[30] T. Lu, F. Chen, Quantitative analysis of molecular surface based on improved Marching Tetrahedra algorithm, J. Mol. Graph. Model. 38 (2012) 314–323.
[31] R.F.W. Bader, M.T. Carroll, J.R. Cheeseman, C. Chang, Properties of atoms in molecules: atomic volumes, J. Am. Chem. Soc. 109 (26) (1987) 7968–7979.
[32] E. Espinosa, I. Alkorta, J. Elguero, E. Molins, From weak to strong interactions: A comprehensive analysis of the topological and energetic properties of the electron density distribution involving X-H··· F–Y systems, J. Chem. Phys. 117 (2002) 5529–5542.
[33] E.D. Glendening, J.K. Badenhoop, A.E. Reed, J.E. Carpenter, J.A. Bohmann, C.M. Morales, P. Karafiloglou, C.R. Landis, F. Weinhold, NBO 7.0, (2018).
[34] J. Klein, H. Khartabil, J.-C. Boisson, J. Contreras-García, J.-P. Piquemal, E. Hénon, New way for probing bond strength, J. Phys. Chem. A, 124 (9) (2020) 1850–1860.
[35] C. Lefebvre, G. Rubez, H. Khartabil, J.-C. Boisson, J. Contreras-García, E. Hénon, Accurately extracting the signature of intermolecular interactions present in the NCI plot of the reduced density gradient versus electron density, PCCP 19 (27) (2017) 17928–17936.
[36] C. Lefebvre, H. Khartabil, J. Boisson, J. Contreras-García, J. Piquemal, E. Hénon, The independent gradient model: a new approach for probing strong and weak interactions in molecules from wave function calculations, ChemPhysChem 19 (2018) 724–735.
[37] F. Neese, WIREs Comput. Mol. Sci. 8 (2017) e1327.
[38] W. Humphrey, A. Dalke, K. Schulten, VMD: visual molecular dynamics, J. Mol. Graph. 14 (1996) 33–38.
[39] K. Imato, K. Ohira, M. Yamaguchi, T. Enoki, Y. Ooyama, Phenazine-based photosensitizers for singlet oxygen generation, Mater. Chem. Front. 4 (2) (2020) 589–596.
[40] B. Martins Estevão, F. Cucinotta, N. Hioka, M. Cossi, M. Argeri, G. Paul, L. Marchese, E. Gianotti, Rose Bengal incorporated in mesostructured silica nanoparticles: structural characterization, theoretical modeling and singlet oxygen delivery, PCCP 17 (2015) 26804–26812.
[41] M. Gierada, F. De Proft, M. Sulpizi, F. Tielens, Understanding the acidic properties of the amorphous hydroxylated silica surface, J. Phys. Chem. C 123 (28) (2019) 17343–17352.
[42] L.T. Zhuravlev, The surface chemistry of amorphous silica. Zhuravlev model, Colloids Surf. A 173 (1-3) (2000) 1–38.
[43] X. Li, X. Du, J. He, Self-cleaning antireflective coatings assembled from peculiar mesoporous silica nanoparticles, Langmuir 26 (16) (2010) 13528–13534.
[44] D. Sriramulu, E.L. Reed, M. Annamalai, T.V. Venkatesan, S. Valiyaveettil, Synthesis and characterization of superhydrophobic, self-cleaning NIR-reflective silica nanoparticles, Sci. Rep. 6 (2016) 35993.
[45] S. Xiao, A. Shoaib, J. Xu, D. Lin, Mesoporous silica size, charge, and hydrophobicity affect the loading and releasing performance of lambda-cyhalothrin, Sci. Total Environ. 831 (2022), 154914.
[46] X. Du, Y.i. Xing, X. Li, H. Huang, Z. Geng, J. He, Y. Wen, X. Zhang, Broadband antireflective superhydrophobic self-cleaning coatings based on novel dendritic porous particles, RSC Adv. 6 (10) (2016) 7864–7871.

[47] C. Deng, Y. Liu, F. Zhou, M. Wu, Q. Zhang, D. Yi, W. Yuan, Y. Wang, Engineering of dendritic mesoporous silica nanoparticles for efficient delivery of water-insoluble paclitaxel in cancer therapy, J. Colloid Interface Sci. 593 (2021) 424–433.
[48] Y. Wang, X. Du, Z. Liu, S. Shi, H. Lv, Dendritic fibrous nano-particles (DFNPs): rising stars of mesoporous materials, J. Mater. Chem. A 7 (2019) 5111–5152.
[49] M.C. Biesinger, X-ray Photoelectron Spectroscopy (XPS) Reference Pages, (2021). http://www.xpsfitting.com/ (accessed November 9, 2022).
[50] B. Bhushan, K.J. Kwak, S. Gupta, S.C. Lee, Nanoscale adhesion, friction and wear studies of biomolecules on silane polymer-coated silica and alumina-based surfaces, J. R. Soc. Interface 6 (37) (2009) 719–733.
[51] M.A. Rauf, J.P. Graham, S.B. Bukallah, M.A.S. Al-Saedi, Solvatochromic behavior on the absorption and fluorescence spectra of Rose Bengal dye in various solvents, Spectrochim. Acta A Mol. Biomol. Spectrosc. 72 (1) (2009) 133–137.
[52] J.C.S. Terra, A. Desgranges, Z. Amara, A. Moores, Photocatalysis on magnetic supports for singlet oxygen generation: role of immobilization and photobleaching, Catal. Today 407 (2023) 52–58.
[53] C. Mendoza, N. Emmanuel, C.A. Páez, L. Dreesen, J.-C. M. Monbaliu, B. Heinrichs, Improving continuous flow singlet oxygen photooxygenation reactions with functionalized mesoporous silica nanoparticles, ChemPhotoChem 2 (10) (2018) 890–897.
[54] J. Ryu, J. Yun, J. Lee, K. Lee, J. Jang, Hierarchical mesoporous silica nanoparticles as superb light scattering materials, Chem. Commun. 52 (10) (2016) 2165–2168.
[55] G. Oster, G. Kallmann Oster, G. Karg, Extremely long-lived intermediates in photochemical reactions of dyes in non-viscous media, J. Phys. Chem. 66 (1962) 2514–2517.
[56] S.M. Linden, D.C. Neckers, Bleaching Studies of Rose Bengal Onium Salts, J. Am. Chem. Soc. 110 (1988) 1257–1260.
[57] A. Zakrzewski, D.C. Neckers, Bleaching Products of Rose Bengal Under Reducing Conditions, Tetrahedron 43 (20) (1987) 4507–4512.